How to cite: *Angew. Chem. Int. Ed.* **2022,** *61,* e202116170
International Edition: doi.org/10.1002/anie.202116170
German Edition: doi.org/10.1002/ange.202116170

Nanozymes

# Guided Synthesis of a Mo/Zn Dual Single-Atom Nanozyme with Synergistic Effect and Peroxidase-like Activity

*Chong-Bo Ma, Yaping Xu, Lixin Wu, Quan Wang, Jia-Jia Zheng, Guoxi Ren, Xiaoyu Wang, Xingfa Gao, Ming Zhou,* Ming Wang,* and Hui Wei**

**Abstract:** We present a facile route towards a dual single-atom nanozyme composed of Zn and Mo, which utilizes the non-covalent nano-assembly of polyoxometalates, supramolecular coordination complexes as the metal-atom precursor, and a macroscopic amphiphilic aerogel as the supporting substrate. The dual single-atoms of Zn and Mo have a high content (1.5 and 7.3 wt %, respectively) and exhibit a synergistic effect and a peroxidase-like activity. The Zn/Mo site was identified as the main active center by X-ray absorption fine structure spectroscopy and density functional theory calculation. The detection of versatile analytes, including intracellular $H_2O_2$, glucose in serum, cholesterol, and ascorbic acid in commercial beverages was achieved. The nanozyme has an outstanding stability and maintained its performance after one year's storage. This study develops a new peroxidase-like nanozyme and provides a robust synthetic strategy for single-atom catalysts by utilizing an aerogel as a facile substrate that is capable of stabilizing various metal atoms.

## Introduction

Metal catalysts supported on a substrate exhibiting high catalytic efficiency have been widely employed in industry,[1] but mainly in cases where the active center only occupies a very limited portion of the total metal atoms.[2] As a "rising star" in catalysis, single-atom catalysts (SACs) have drawn substantial attention in heterogeneous catalysis research because of the superiority in maximized atomic utilization and unsaturated coordination.[3] To date, various synthetic approaches for SACs have been demonstrated, under which numerous SACs have been successfully produced. Previous examples confirm that the catalytic performance of a SAC is strongly dependent on the coordination circumstances,[4] an intimate interaction between metal atoms and the support,[5] and the loading amount of the metal atoms.[6] Increase of the metal loading while conserving the dispersal status of the metal atoms is a recognized strategy to improve the performance. However, the atomically dispersed metals have a sharp increase in their surface free energy, resulting in the extreme ease of site aggregation into particle size with attenuated activity.[2] In spite of the efforts devoted to the fabrication of SACs, like the defect construction on metal hydroxide/oxide supports,[7] nanospace confinement,[8] and employment of strengthened interactions between metal atoms and coordinating heteroatoms,[9] these strategies still have their own demerits. For example, the pyrolysis treatment of metal organic frameworks (MOFs) often causes structural collapse of MOFs and leads to shrunken volume, which is not favorable to single dispersion of metal atoms.[10] Sometimes, an acid etching process is required to remove the non-single metallic species, which would impair the loading amount of the single atoms.[11] Moreover, the stabilizing sites on the substrate are usually required to be carefully engineered, and in most conditions the nanoscale size of the substrates also limits the loading amount of the metal atoms. These features explain the reason why current SACs exhibit low atom loading (<2 wt%). Taking the

[*] Dr. C.-B. Ma, Dr. M. Zhou
Key Laboratory of Polyoxometalate and Reticular Material Chemistry of Ministry of Education, National & Local United Engineering Laboratory for Power Batteries, Key Laboratory of Nanobiosensing and Nanobioanalysis at Universities of Jilin Province, Analysis and Testing Center, Department of Chemistry, Northeast Normal University, Changchun, Jilin Province 130024 (China)
E-mail: zhoum739@nenu.edu.cn

Y. Xu, Dr. L. Wu, Dr. M. Wang
State Key Laboratory of Supramolecular Structure and Materials, College of Chemistry, Jilin University, Changchun, 130012 (China)
E-mail: mingwang358@jlu.edu.cn

Q. Wang, Dr. X. Wang, Dr. H. Wei
Department of Biomedical Engineering, College of Engineering and Applied Sciences, Nanjing National Laboratory of Microstructures, Jiangsu Key Laboratory of Artificial Functional Materials, Nanjing University, Nanjing, Jiangsu 210023 (China)
and
State Key Laboratory of Analytical Chemistry for Life Science and State Key Laboratory of Coordination Chemistry, School of Chemistry and Chemical Engineering, Chemistry and Biomedicine Innovation Center (ChemBIC), Nanjing University, Nanjing, Jiangsu 210023 (China)
E-mail: weihui@nju.edu.cn

Dr. J.-J. Zheng, Dr. X. Gao
Laboratory of Theoretical and Computational Nanoscience, National Center for Nanoscience and Technology of China, Beijing, 100190 (China)

Dr. G. Ren
State Key Laboratory of Functional Materials for Informatics, Shanghai Institute of Microsystem and Information Technology, Chinese Academy of Sciences, Shanghai 200050 (China)

dimension of the substrate into account, we consider that the utilization of a substrate with macroscopic dimension may be a way to practically increase the loading amount of the metal atoms, preferably with the capacity to stabilize various metal atoms simultaneously.

Heteroatoms (O, N, or S, etc.) have been confirmed to have the ability to stabilize the single-atom species.[9] Hence, a macroscope aerogel with an abundance of heteroatoms on the surface may be an ideal candidate. Benefitting from the richness in hydroxyl groups (-OH), the aerogel product based on poly(vinyl alcohol) (PVA) has an abundance of oxygen-containing groups (ester, epoxy, and hydroxyl groups, etc.) on the surface.[12] PVA is accessible through a straightforward synthesis route and the raw materials are low-cost and widely available. Moreover, the self-assembling process of the PVA chain under hydrothermal conditions allows for easy tuning of the pore size of the aerogel. The surface groups together with the tunable pore size can provide the complexation sites as well as the spatial confinement effect for metal atoms. As a three-dimensional macroscope substrate, such an aerogel is expected to work as a novel stabilizing support for SACs. It has been previously reported that dual single atoms exhibit a synergistic effect in catalysis,[13] hence, to verify the feasibility and flexibility of the aerogel in stabilizing different metal atoms, a precursor with two distinct metals is a preferred choice.

Polyoxometalates (POMs), composed of metal oxide clusters, are a class of nanoscaled molecular metal oxides with redox activity.[14] POMs are always connected with other materials through covalent or non-covalent interactions to achieve certain functionalities, such as tailoring electrochemical properties, for example.[15] Amongst them, electrostatic interactions provide a vast platform for the combination of the negatively charged POMs with diverse cationic species.[16] Discrete supramolecular frameworks consisting of explicit coordination sites as the constitutional units, possess rigorous structures and precise positive charges. Previous research has indicated that in such inorganic–organic arrangements with different structural features, thermal and electrochemistry properties can be induced.[17] There are many reports on non-covalent assembly of such anions and cations, which have resulted in materials with desirable properties.[18] Hence, we conceived the idea of utilizing the non-covalent assembly of supramolecular coordination complexes (SCCs) and POMs to guide the synthesis of SACs in a controlled manner, preferably yielding dual single-atoms with a synergistic effect assisted by the intimate relationship between the SCCs and POMs.

Herein, we employed the nano assembly of SCCs and POMs (NSPs) as the metal precursor, the amphiphilic PVA aerogel as the substrate to synthesize the dual single-atom catalyst (DSAC). The formation of NSPs relies on the electrostatic interactions between the metallotriangle $\mathbf{[Zn_3L_3][PF_6]_6}$ (L: ligand; structure is shown in Figure S1, in the Supporting Information) (possessing six positive charges) and Lindquist-type POM $\mathbf{[TBA]_2[Mo_6O_{19}]}$ (TBA: tetrabutylammonium) (possessing two negative charges),[19] which were utilized as the Zn and Mo precursors, respectively. Both species are soluble in acetonitrile and the combination of both results in a yellow precipitate that is insoluble in most common solvents. The pre-synthesized amphiphilic aerogel was soaked with the acetonitrile solution of $\mathbf{[Zn_3L_3][PF_6]_6}$ and $\mathbf{[TBA]_2[Mo_6O_{19}]}$, respectively, followed by a pyrolysis process at 800 °C in a $N_2$ atmosphere. The resulting product of a Zn/Mo dual single-atom catalyst supported on the macroscope aerogel (Zn/Mo DSAC-SMA) was obtained without post-treatment, thus avoiding the acid etching procedure that may decrease the loading amount of the metal atoms. The Zn/Mo DSAC-SMA was found to have remarkable peroxidase (POD)-like activity, and was applied in glucose detection in serum, ascorbic acid (AA) detection in beverage, cholesterol determination, and intracellular $H_2O_2$ detection (Scheme 1).

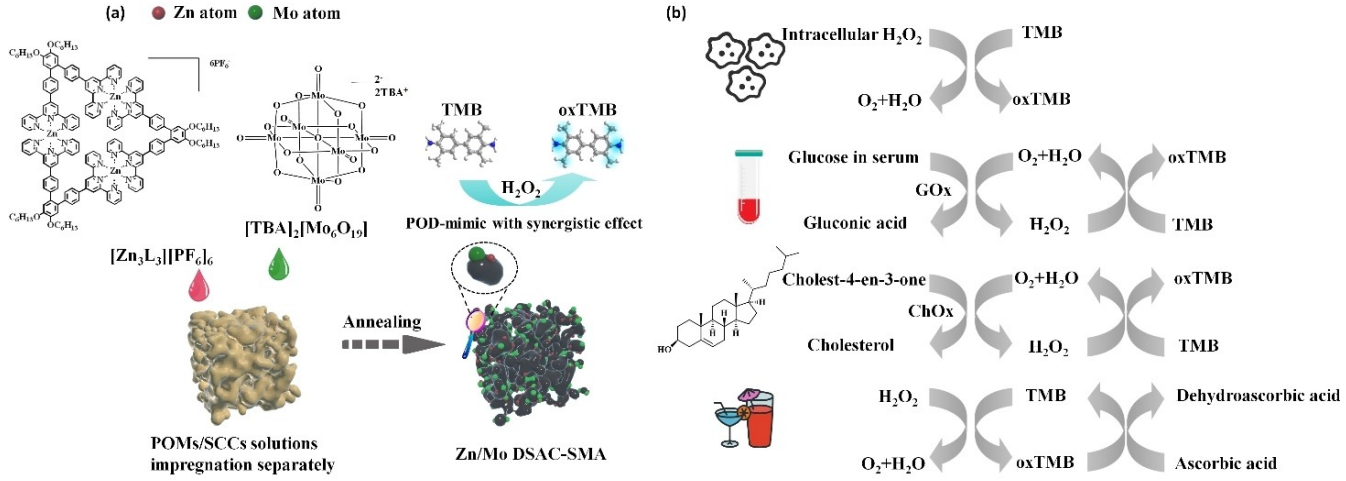


***Scheme 1.*** a) Schematic illustration of the fabrication process of the confined Zn/Mo dual single-atom nanozyme loaded on PVA-based aerogel; b) Versatile applications in intracellular $H_2O_2$ detection, glucose detection in serum, cholesterol determination, and ascorbic acid in beverage detection.

## Results and Discussion

The aerogel substrate is flexible in tuning of the pore size and surface chemistry by altering the concentration of PVA precursor and the dosage ratio between PVA and maleic acid (MA).[12b,c] To equip the aerogel surface with an abundance of oxygen-containing groups to accommodate the single-atom sites, the MA dosage was determined to make the total number of –COOH groups in the MA molecule 50 % of that of the –OH groups on the PVA chain, in theory. The pristine aerogel (PA) possesses a continuous porous structure as shown in Figure S2a, b in the Supporting Information. In the absence of the aerogel, the combination between $\mathbf{[Zn_3L_3][PF_6]_6}$ and $\mathbf{[TBA]_2[Mo_6O_{19}]}$ yields a product with rod-like structure (Figure S3a, Supporting Information). However, when $\mathbf{[Zn_3L_3][PF_6]_6}$ and $\mathbf{[TBA]_2[Mo_6O_{19}]}$ infiltrate the aerogel successively, they interact with each other and the NSPs were formed in situ, showing spheroidal structures (Figure S3b, Supporting Information). This phenomenon indicates the spatial confinement and complexation effect provided by the aerogel. The pyrolyzed pristine aerogel (PPA) can preserve its porous structure and three-dimensional (3D) character without structural collapse (Figure S4, Supporting Information). Such a feature lays the foundation of effective loading and increase in the loading amount of metal single atoms. The NSPs-loaded aerogel was transformed into the final product after the pyrolysis process at 800 °C for 30 min. PA, PAA, NSPs-loaded aerogel, and Zn/Mo DSAC-SMA were characterized by Fourier transform infrared (FT-IR) spectroscopy (Figure 1a). For PA and NSPs-loaded aerogel, the remarkable absorption band around $\approx$2925 $cm^{-1}$ and $\approx$1706 $cm^{-1}$ can be assigned to aliphatic $–CH_2–$[29] on the PVA chain and –COOH on aerogel surface,[12b] respectively, which are not present for PAA and Zn/Mo DSAC-SMA. The grey area in the spectral region indicates the existence of aromatic C=C stretching[30] in the three samples except PA. For PAA and Zn/Mo DSAC-SMA, this results from the pyrolysis process, and for the NSPs-loaded aerogel, it comes from the NSPs encapsulated in the aerogel matrix. The characteristic bands for $PF_6^-$[31] and Mo–O stretching[32] can be easily identified for the NSPs-loaded aerogel, of which the former bands almost disappear in Zn/Mo DSAC-SMA, and the latter bands are weakened, suggesting the presence of a Mo–O bond in the Zn/Mo DSAC-SMA product. Notably, the faint absorption band at 560–660 $cm^{-1}$ suggests the existence, but small quantity, of an Mo–N moiety.[33] Aberration-corrected high-angle annular darkfield scanning transmission electron microscopy (HAADF STEM) was utilized to investigate the local distribution of Zn and Mo atoms. Figure 1b is the high-magnification STEM image of the red square region in Figure 1d, which shows a dense distribution of the single atoms, whereas Figure 1c presents a sparse scene. Although it is hard to differentiate Zn and Mo atoms owing to their

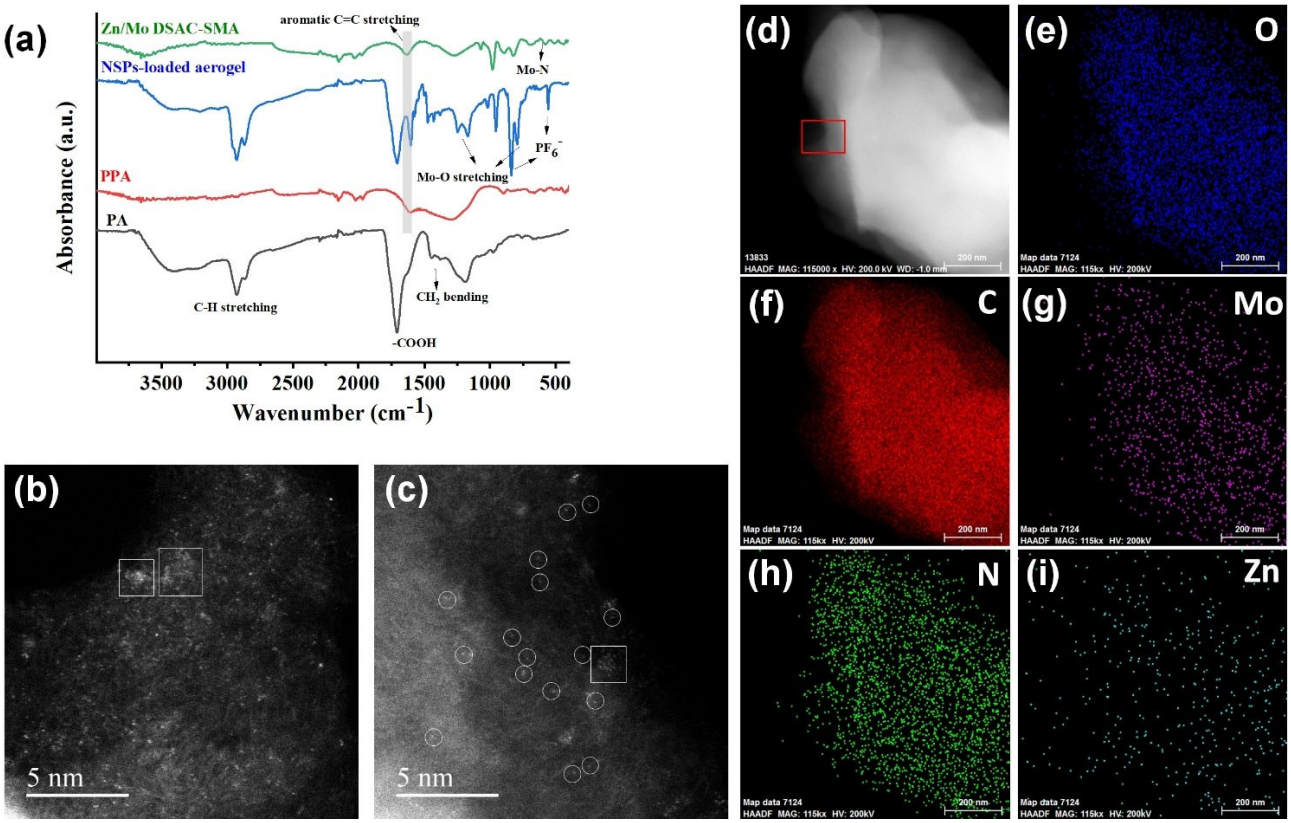


*Figure 1.* a) FT-IR spectra for PA, PAA, NSPs-loaded aerogel, and Zn/Mo DSAC-SMA; b, c) STEM images of Zn/Mo DSAC-SMA. The white circles highlight single Zn or Mo atoms, and the white squares indicate clusters; b) is the high-magnification STEM image of the red square region in (d). d–i) Elemental mapping of Zn/Mo DSAC-SMA by energy-dispersive X-ray spectroscopy.

close atomic numbers, Mo atoms are brighter than Zn atoms and the single-dispersed atoms are distinctly recognized with merely a small number of clusters noticed (indicated by the white squares in Figure 1b,c). Elemental mapping confirms the homogeneous distribution of Zn, Mo, O, and N over the aerogel surface (Figure 1d–i). Simultaneously, these results indicate that the loading amount of Zn is lower than that of Mo. The ICP-atomic emission spectroscopy (ICP-AES) measurement verified this finding, showing the metal loadings of Zn and Mo as 1.5 and 7.3 wt%, respectively. In terms of metal loading, our material is superior to most previous reports on Zn- or Mo-based single-atom materials (Table 1). Such a delightful feature originates from the competence of the aerogel as the supporting substrate for single metal atoms. The self-equipped oxygen-containing groups as well as the continuous pores can provide the coordination sites for the atoms, avoiding the acid etching procedure that may violate high metal loading. The firm aerogel skeleton maintains a three-dimensional feature without structural collapse after pyrolysis at high temperature and has a surface area of 203.3 $m^2 g^{-1}$ according to the Brunauer–Emmett–Teller (BET) test. Compared with previous efforts in improving the atom loading, such as the versatile multilayer stabilization approach,[34] our system provides a more straightforward and cost-effective route to reach this goal.

We utilized X-ray absorption fine structure (EXAFS) spectroscopy to acquire the coordination chemistry of the samples. According to the EXAFS spectra from the K-edge of Mo and Zn, information about the coordination environment of the central Mo/Zn atoms can be acquired. As shown in Figure 2a,b and Table S1, the structures of Zn–$N_{5.6}$, Mo–$N_{2.9}$, Mo–$O_{2.3}$, and Mo–$Zn_{0.54}$ correspond to an adequate fitting. These results indicate that the Mo and Zn atoms are atomically distributed on the aerogel substrate. From the X-ray photoelectron spectroscopy (XPS), the binding energies (BEs) of 235.2 and 232.1 eV in the high-resolution Mo 3d spectrum can be assigned to $Mo^{VI}$ $3d_{3/2}$ and Mo $3d_{5/2}$, respectively (Figure 2c).[35] The peaks at 1044.9 and 1021.8 eV correspond to Zn $2p_{1/2}$ and Zn $2p_{3/2}$[36] (Figure 2d).

***Table 1:*** Comparison of the Zn or Mo single-atom content between previous studies and our work.

| Materials | Single-atom content [wt%][a] | | References |
|---|---|---|---|
| | Zn | Mo | |
| Zn-TpPa | 0.5 | N.A. | [20] |
| $0.2Zn_1$-$Sn_1$/CuO | 0.2 | N.A. | [21] |
| $ZnN_x$/C | 0.1 | N.A. | [22] |
| $ZnN_x$/BP | 1 | N.A. | [23] |
| Mo-NP/AC | N.A. | 3.72 | [24] |
| Mo–SAs | N.A. | 1.32 | [25] |
| Mo–O/N–C | N.A. | 0.4 | [26] |
| Co–Mo–S | N.A. | 0.3 | [27] |
| $Mo_{SA}$–$N_3$–C | N.A. | 0.83 | [28] |
| $W_1Mo_1$–NG | N.A. | 2.55 | [13b] |
| $Ir_1Mo_1/TiO_2$ | N.A. | 0.06 | [13a] |
| Zn/Mo DSAC-SMA | 1.5 | 7.3 | This work |

[a] N.A. = not available.

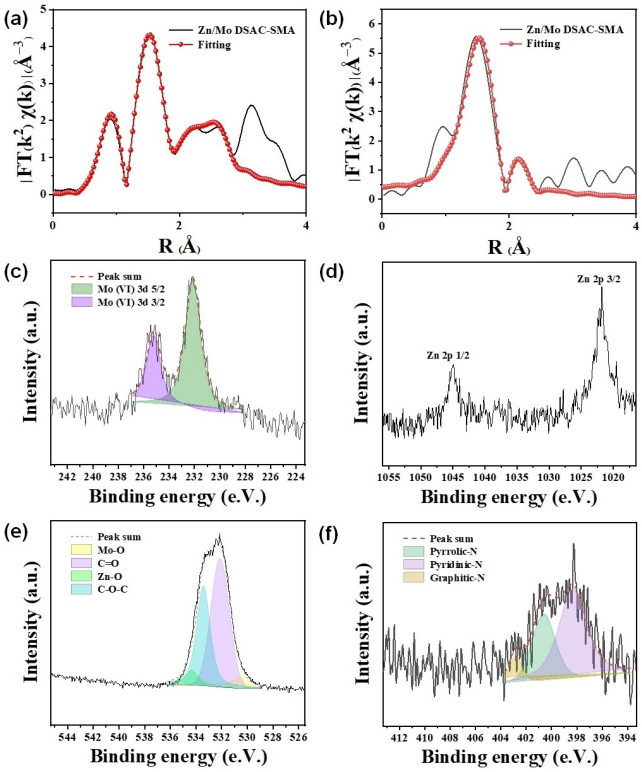


***Figure 2.*** The fitting curves of the EXAFS spectra in R-space for a) Mo and b) Zn, and the XPS spectra of Zn/Mo DSAC-SMA c) Mo 3d, d) Zn 2p, e) O 1s and f) N 1s.

The slightly lower BE than the standard one for ZnO (1022 eV)[37] may indicate the existence of some Zn–N bonds in Zn/Mo DSAC-SMA. Such a decrease in BE is ascribed to the decrease in ionicity, and for Zn–N, the ionicity is weaker than that for Zn–O according to the Pauling theory.[23,37,38] The O 1s spectrum deconvoluted into four individual peaks at 534.3, 533.4, 532.1 and 530.6 eV can be correlated to the Zn–O bond,[20] C–O–C/C=O[39] and Mo–O bond,[24,40] respectively (Figure 2e). In the deconvoluted spectrum of nitrogen, three peaks at 398.3, 400.6 and 402.8 eV are responsible for pyridinic-N, pyrrolic-N, and graphitic-N[41] (Figure 2f). Previous studies have concluded that pyridinic-N and pyrrolic-N are capable of stabilizing atomically dispersed Zn[23] or Mo[28] metals. Such results reveal the talent of NSPs as a precursor of SACs by virtue of intrinsic possession of the ability to stabilize metal single atoms.

The POD-like activity of Zn/Mo DSAC-SMA was systematically investigated by monitoring the ultraviolet-visible (UV/Vis) absorbance at 652 nm for the oxidation form of 3,3′,5,5′-tetramethylbenzidine (TMB) substrates (oxTMB) in the presence of $H_2O_2$ (Figure 3a, black curve). In contrast, the negligible absorbance of the solution containing only Zn/Mo DSAC-SMA and TMB excludes the oxidase (OXD)-like activity of Zn/Mo DSAC-SMA (Figure 3a, red curve). The catalytic activity of free-standing NSPs was also compared and neither POD-like nor OXD-like activity was found, suggesting the negligible activity of

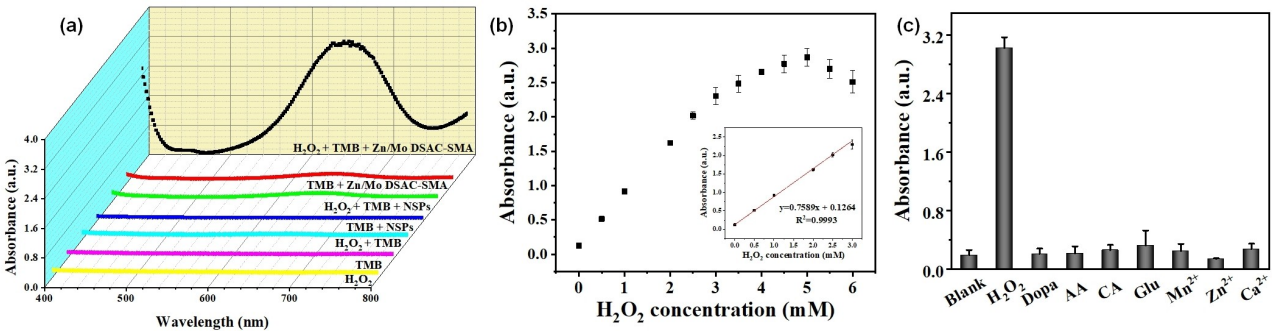


***Figure 3.*** a) UV/Vis absorption spectra comparison for $H_2O_2$ + TMB + Zn/Mo DSAC-SMA, TMB + Zn/Mo DSAC-SMA, $H_2O_2$ + TMB + NSPs, TMB + NSPs, $H_2O_2$ + TMB, TMB, and $H_2O_2$; b) The $H_2O_2$-concentation dependence of the chromogenic reaction with the inset showing the linear relationship in the range of 0–3 mM; c) Selectivity test for $H_2O_2$ detection.

NPSs before pyrolysis (Figure 3a, green and blue curves). Considering that the specific conditions of the pyrolysis process, and the content of the metal atoms are both decisive factors for the catalytic performance, we tried altering the pyrolysis temperature and time, as well as the loading amount of NSPs to seek the optimal activity. It can be concluded that a pyrolysis temperature of 800 °C with a time of 30 min can create the product with best performance (Figure S5, Supporting Information). An excessively high or low loading amount of NSPs would lead to a deterioration in activity. As indicated by the previous report, the monotypic single atom of Zn or Mo was found to have POD-like activity.[28,42] In our research, **$[Zn_3L_3][PF_6]_6$** and **$[TBA]_2[Mo_6O_{19}]$** was solely used to infiltrate the aerogel prior to the pyrolysis to fabricate monotypic single atoms of Zn and Mo, named Zn SAC and Mo SAC, respectively. In order to demonstrate the synergic effect between Zn and Mo atoms, we compared the catalytic performance of Zn SAC, Mo SAC, and their simple mixture. As revealed by Figure S6 in the Supporting Information, the monotypic Zn- and Mo-based SACs are also active as POD mimics, but the performances are only ≈30 % and ≈33 % of Zn/Mo DSAC-SMA. Such a result suggests the indispensable synergic effect between Zn and Mo in this work.

The POD-like activity of Zn/Mo DSAC-SMA is also concentration, pH, and temperature dependent (Figure S7, Supporting Information), as with HRP. The kinetics of the TMB oxidation process catalyzed by Zn/Mo DSAC-SMA was studied by changing the concentration of TMB or $H_2O_2$ while the concentration of the other was sustained. The $K_m$ and $V_{max}$ values were calculated and are listed in Table 2, in which the $k_{cat}/K_m$ values, which have been used to evaluate the catalytic performance,[46] are also exhibited. The Zn/Mo DSAC-SMA has higher $k_{cat}/K_m$ values than those of the nanozymes singly based on zinc or molybdenum elements. Such a result also validates the synergistic effect of Zn and Mo in enhancing the catalytic performance. The double reciprocal plots for the reaction between TMB and $H_2O_2$ showed a set of linear and parallel lines when one concentration was fixed and the other one was varied (Figure S8, in Supporting Information), indicating a ping pong type of mechanism. In terms of the catalytic mechanism, we first investigated whether the reactive oxygen species (ROS) is involved during the reaction. Hydroethidine (HE) was used to detect the production of superoxide anions ($O_2^{\bullet-}$). HE can be oxidized by $O_2^{\bullet-}$ to form a fluorescent compound with red fluorescence (Figure S9a, Supporting Information, red curve). The fluorescence decreased when Zn/Mo DSAC-SMA was introduced, indicating the possible superoxide dismutase (SOD)-like activity of Zn/Mo DSAC-SMA that can scavenge $O_2^{\bullet-}$ rather than produce it (Figure S9a, Supporting Information, black curve). Electron spin resonance (ESR) technology was utilized to detect short-lived free radicals. A 1:1:1 triplet signal with g value of 2.030 was observed when 2,2,6,6-tetramethyl-4-piperidone (TEMP) was present with Zn/Mo DSAC-SMA and $H_2O_2$ (Figure S9b, Supporting Informa-

***Table 2:*** Comparison of the $K_m$, $V_{max}$, $k_{cat}/K_m$ under different substrates between some previous studies and our work.

| Materials | $H_2O_2$ as substrate | | TMB as substrate | | $k_{cat}/K_m$ | | References |
|---|---|---|---|---|---|---|---|
| | $K_m$ [mM] | $V_{max}$ [$10^{-8}$ M $s^{-1}$] | $K_m$ [mM] | $V_{max}$ [$10^{-8}$ M $s^{-1}$] | $H_2O_2$ [$s^{-1}$ $M^{-1}$] | TMB [$s^{-1}$ $M^{-1}$] | |
| Zn/Mo DSAC-SMA | 40.32 | 33.33 | 0.43 | 3.84 | 17.48 (Zn)<br>5.44 (Mo) | 188.80 (Zn)<br>58.79 (Mo) | This work |
| HRP | 3.70 | 8.71 | 0.43 | 10.00 | 0.94 | 9.22 | [43] |
| $Mo_{SA}$–$N_3$–C nanozyme | – | 37 | 0.79 | – | 100 | 75.95 | [28] |
| PMCS | 40.16 | 12.15 | 0.224 | 10.66 | – | – | [44] |
| Zn–N–C-800 | 0.14 | 3.31 | $2.13\times10^{-4}$ | 3.04 | 0.014 | 8.5 | [45] |
| FeBNC | – | – | – | – | 14.65 | 234.23 | [46] |

tion), and suggests the formation of singlet oxygen ($^1O_2$) species in the system.

Taking advantage of the remarkable POD-like activity, the colorimetric detection of $H_2O_2$ has been realized. The absorbance caused by the produced oxTMB gradually increased with the increasing concentration of $H_2O_2$ (Figure 3b), with a linear relationship in the range of 0–3 mM, from which a limit of detection (LOD) of 24.4 μM can be acquired (Figure 3b, inset). Dopamine (dopa), ascorbic acid (AA), citric acid (CA), glucose (glu), $Mn^{2+}$, $Zn^{2+}$, and $Ca^{2+}$ were employed as some possible interference substances in $H_2O_2$ detection, none of which interfered with the detection (Figure 3c). The detection of $H_2O_2$ produced by Hela cells was achieved by short-term stimulation of Hela cells with phorbol-12-myristate-13-acetate (PMA). The generated $H_2O_2$ was transformed by Zn/Mo DSAC-SMA into $^1O_2$, which can induce the formation of oxTMB. A cell number of $10^5$ produces a colorimetric response under PMA stimulation. An absorbance value of 0.24 was obtained, which can be utilized to calculate the average amount of $H_2O_2$ released by a single cell to be $1.72\times10^{11}$. This result is consistent with those reported previously.[47]

To understand the catalytic mechanism and identify the active center, density functional theory (DFT) calculations were performed. The plausible reaction pathways for POD-like nanozymes were proposed as shown in Figure 4a. In both pathways, the hydroxyl-adsorbed structure is one of the key intermediates and the –OO– adsorbate in the pathway may yield the ESR signal of $^1O_2$ in the presence of TEMP, as observed experimentally. According to previous theoretical studies, the adsorption energy of hydroxyl ($\boldsymbol{E_{ads,OH}}$) could be a descriptor for the catalytic performance of POD-like nanozymes.[48] The POD activity window defined by $\boldsymbol{E_{ads,OH}}$ was −3.5 to −1.6 eV and the optimal value of $\boldsymbol{E_{ads,OH}}$ was predicted to be −2.6 eV. The DFT-calculated $\boldsymbol{E_{ads,OH}}$ suggests that the dual Zn/Mo site is better than the other two single-atom sites, because its $\boldsymbol{E_{ads,OH}}$ (−3.01 eV) is closer to the optimal value than the other two (−2.17 eV and −3.44 eV for Zn SAC and Mo SAC, respectively; Figure 4b–d). These results indicate that the combination of Zn and Mo sites synergistically improved the POD-like activity. Another possible explanation for the synergetic effect in Zn/Mo DSAC-SMA is that $H_2O_2$ dissociation occurs easily on the Mo site owing to its strong affinity to hydroxyl species. Then, the hydroxyl migrates to the Zn site, which usually occurs with a small energy barrier. Finally, it reacts with TMB to form $H_2O$ and oxTMB. The Zn site has a weaker hydroxyl affinity, therefore, such a reaction could be possible with a smaller barrier. As a result, the overall POD-like activity was improved.

Based on the POD-like activity, we also demonstrated the applicability of Zn/Mo DSAC-SMA in the detection of glucose and cholesterol, with the aid of glucose oxidase (GOx) and cholesterol oxidase (ChOx), respectively. Glucose detection was accomplished following one- and two-step strategies, whereas cholesterol detection was accomplished through a two-step method owing to the distinct optimal pH environments for ChOx and Zn/Mo DSAC-SMA. For glucose, the linear ranges from 0–1 mM and 0–1.8 mM were obtained with LODs by one- and two-step strategies of 21.4 μM and 15.6 μM, respectively (Figure 5a, b). The cholesterol detection exhibited a linear range of 0–250 μM and a LOD of 7.44 μM (Figure 5c). The glucose detection in diluted human serum (1 % and 2 %) has a high recovery rate (Table 3), further suggesting the practicality in real sample detection.

AA, an antioxidant that can scavenge free radicals, is able to impede the chromogenic reactions triggered by a nanozyme. When AA is pre-added into the Zn/Mo DSAC-SMA/TMB/$H_2O_2$ mixture, the production of oxTMB will be inhibited leading to rapid decrease in absorbance at 652 nm (Figure 6a). The AA detection has a wide detection range from 0.1–5000 μM with two linear ranges of 0.1–1000 μM and 1000–5000 μM (Figure 6b, c) and a LOD of 0.76 μM. Some potential interfering substances (including histidine, glutamic acid, leucine, alanine, phenylalanine, tryptophan, threonine, valine, cysteine, glucose, maltose, fructose, glycine, saccharose, $Na^+$, and $K^+$) were employed to investigate the selectivity in AA detection. Most of them posed no interference towards the detection except cysteine (Figure 6d). Some commercial beverages that contain AA were used as the real samples to manifest the competence of Zn/

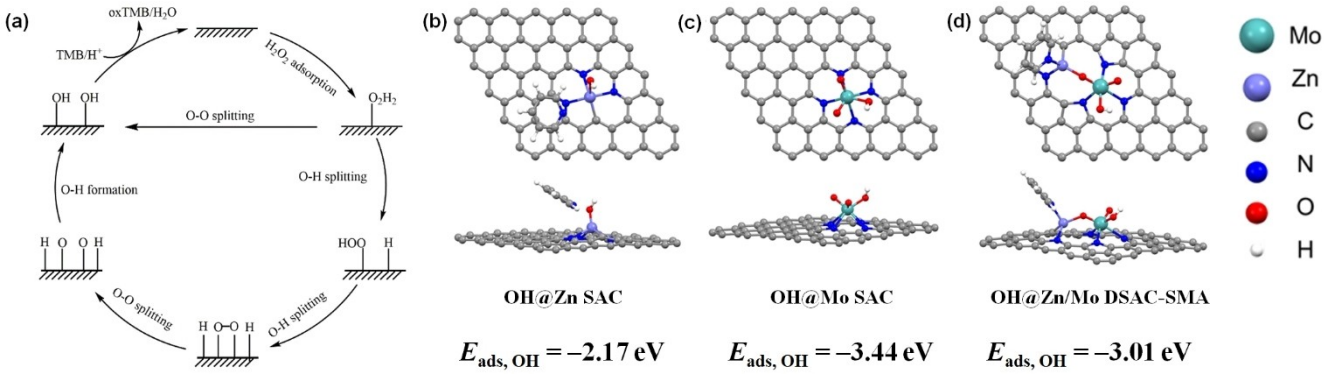


***Figure 4.*** a) Proposed reaction pathways for POD-like nanozymes. Computational models and optimized hydroxyl adsorption structures at the b) Zn-SAC, c) Mo-SAC, and d) Zn/Mo DSAC-SMA active sites (top view and side view). The corresponding adsorption energy of hydroxyl ($\boldsymbol{E_{ads,OH}}$) for each site is listed at the bottom.

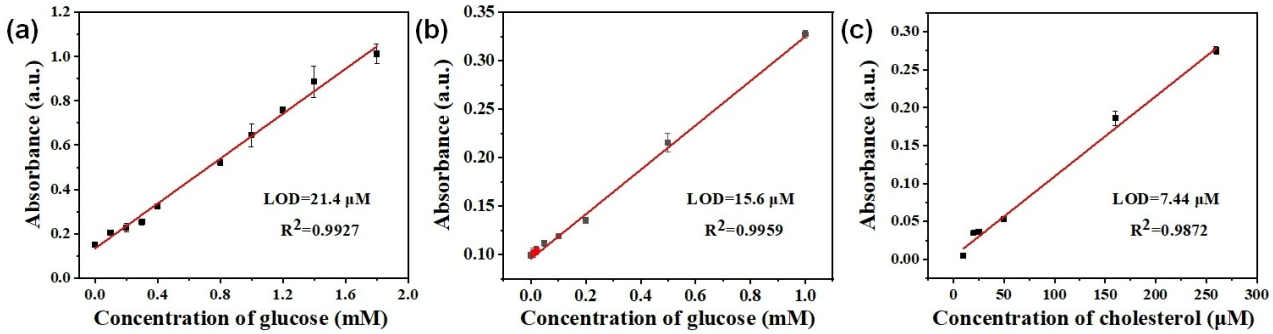


***Figure 5.*** The linear ranges for a) one- and b) two-step detection of glucose and c) detection of cholesterol.

***Table 3:*** Glucose detection results in different concentrations of human serum.

| Samples | Added glucose [mM] | Found [mM] | Recovery rate [%] |
|---|---|---|---|
| 1% human serum (0.083 mM) | 0 | 0.088 ± 0.001 | 106.0 |
| | 0.2 | 0.292 ± 0.031 | 103.2 |
| | 1 | 1.240 ± 0.072 | 114.5 |
| 2% human serum (0.166 mM) | 0 | 0.191 ± 0.007 | 115.1 |
| | 0.2 | 0.392 ± 0.019 | 107.1 |
| | 1 | 1.250 ± 0.002 | 107.2 |

Mo DSAC-SMA in AA detection. To comfirm the dependability of the standard curves, as well as the applicability of Zn/Mo DSAC-SMA in real sample detection, the real samples were prepared by diluting the beverages to a low concentration and also with the extra addition of AA to a high concentration, both of which exhibited a satisfactory recovery rate (Table 4).

Another notable feature of Zn/Mo DSAC-SMA is the super long-term stability, including both the structural stability and the long-term durable performance for catalysis. For the Zn/Mo DSAC-SMA sample that was extracted by freeze-drying after being immersed in water for a time of one year, the dense distribution of the single atoms can be easily spotted (Figure S10, in Supporting Information). Such an observation verifies the capacity of the aerogel substrate in stabilizing the dual single atoms of Zn and Mo. The durable catalytic performance was evidenced by both catalyzing the reaction between TMB and $H_2O_2$ (Figure 7a) and the detection of AA with concentrations of 0.01 mM and 2 mM (Figure 7b), using the Zn/Mo DSAC-SMA newly made, six months old, and one year old. No attenuation in the performance was observed, indicating the excellent stability of the material. Such a feature has rarely been reported in the previous reports, demonstrating the great

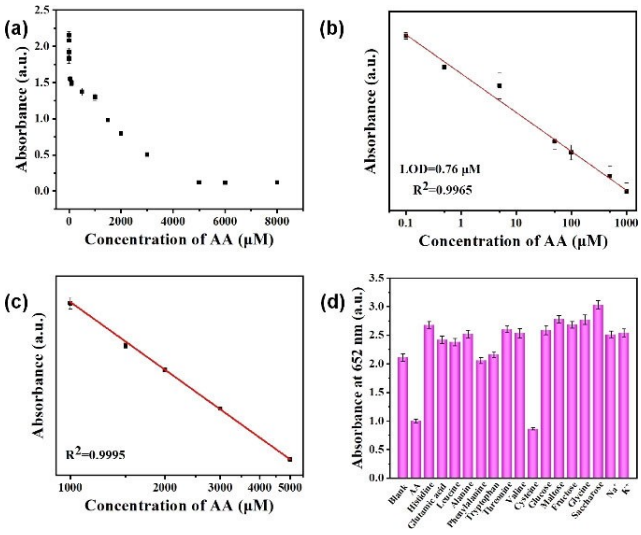


***Figure 6.*** a) The attenuation of the absorbance with the increasing concentration of AA; linear ranges for AA detection: b) 0.1–1000 μM and c) 1000–5000 μM; d) Selectivity test for AA detection.

***Table 4:*** AA detection results in different commercial beverages.

| | Beverage 1 [%] | Beverage 2 [%] | Beverage 3 [%] | Beverage 4 [%] | Beverage 5 [%] |
|---|---|---|---|---|---|
| Recovery rate (Diluted sample) | 100.14 | 101.05 | 101.95 | 101.05 | 102.22 |
| Recovery rate (Standard addition) | 97.48 | 98.29 | 98.47 | 99.06 | 97.90 |

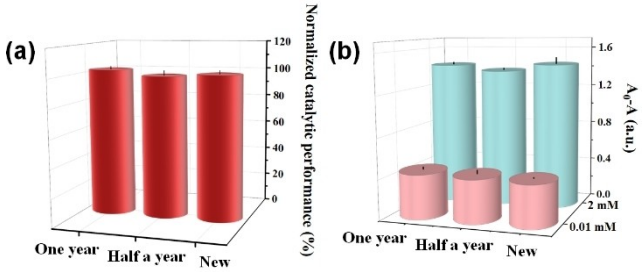


***Figure 7.*** Performance comparison in a) catalyzing the reaction between TMB and $H_2O_2$ (the performance of newly made Zn/Mo DSAC-SMA was regarded as 100%); b) the detection of AA with concentrations of 0.01 and 2 mM, using the Zn/Mo DSAC-SMA that was one year old, six months old, and new.

feasibility of our synthetic strategy for the fabrication of other single-atom-based catalysts with a long-lasting storage stability.

## Conclusion

In summary, we utilized the non-covalent nano-assembly of POMs and SCCs as the metal precursors, and the 3D macroscope amphiphilic aerogel as the supporting substrate to prepare a Zn/Mo dual single-atom catalyst. The aerogel has intrinsically oxygen-containing groups on the surface that work as the complexing sites and has a tunable pore size that provides a spatial confinement effect for metal atoms. The singly dispersed metal atoms are readily acquired after the pyrolysis process without either an acid etching procedure or the structural collapse of the aerogel, which promotes a high loading amount of the metal atoms (Zn 1.5 wt%, Mo 7.3 wt%). The XAFS and DFT calculations jointly revealed that the Zn/Mo site is the main active center and the synergistic effect between Zn and Mo atoms leads to the superior activity of the Zn/Mo DSAC-SMA. More impressive, the nanozyme possesses a super-long stability so that the catalytic performance is maintained for more than one year. The detection of versatile analytes including intracellular $H_2O_2$, glucose in serum, cholesterol, and the ascorbic acid in commercial beverages are realized. Our report not only proposes a new-type of nanozyme as a POD mimic with a super long-term stability, but also provides a novel synthesis strategy for single-atom catalysts by making full use of the unique architecture of POMs and SCCs to facilitate the formation of metal single atoms and the peculiar surface state of polymer-based aerogels to stabilize the metal atoms. The conceptual synthesis approach is also expected to provide the possibility to stabilize other categories of metal atoms and extend the design strategy for nanozymes and other single-atom catalysts.

## Acknowledgements

This work was supported by the National Natural Science Foundation of China (22004014), the National Key Research and Development Project of China (2020YFA0406101), the Natural Science Foundation of Jilin Province, China (No. 212558JC010484610), the Fundamental Research Funds for the Central Universities (No. 2412020QD007, JGPY201802, 2412020ZD006 and 2412019QD008), Human Resources and Social Security Department of Jilin Province, the "111" Project (China, No. B18012), the Jilin Provincial Department of Education (China), the National Key R&D Program of China (2019YFA0709200), and the Analysis and Testing Center of Northeast Normal University (China). We also thank Ms. Yu Zhang and Prof. Yan Du in Changchun Institute of Applied Chemistry, Chinese Academy of Sciences, for their help in organizing the manuscript and data processing. We thank beamline BL14W1 (Shanghai Synchrotron Radiation Facility) for providing the beam time.

## Conflict of Interest

The authors declare no conflict of interest.

## Data Availability Statement

The data that support the findings of this study are available from the corresponding author upon reasonable request.

**Keywords:** Aerogel Substrates · Dual Single Atoms · Nanozymes · Peroxidase · Synergy Effect

[1] P. He, B. Xu, X. Xu, L. Song, X. Wang, *Chem. Sci.* **2016**, *7*, 1011–1015.
[2] X.-F. Yang, A. Wang, B. Qiao, J. Li, J. Liu, T. Zhang, *Acc. Chem. Res.* **2013**, *46*, 1740–1748.
[3] a) A. Beniya, S. Higashi, *Nat. Catal.* **2019**, *2*, 590–602; b) X. Cui, W. Li, P. Ryabchuk, K. Junge, M. Beller, *Nat. Catal.* **2018**, *1*, 385–397; c) Y. Shi, Z.-R. Ma, Y.-Y. Xiao, Y.-C. Yin, W.-M. Huang, Z.-C. Huang, Y.-Z. Zheng, F.-Y. Mu, R. Huang, G.-Y. Shi, Y.-Y. Sun, X.-H. Xia, W. Chen, *Nat. Commun.* **2021**, *12*, 3021.
[4] a) Y. Pan, Y. Chen, K. Wu, Z. Chen, S. Liu, X. Cao, W.-C. Cheong, T. Meng, J. Luo, L. Zheng, C. Liu, D. Wang, Q. Peng, J. Li, C. Chen, *Nat. Commun.* **2019**, *10*, 4290; b) Y. Ren, Y. Tang, L. Zhang, X. Liu, L. Li, S. Miao, D. S. Su, A. Wang, J. Li, T. Zhang, *Nat. Commun.* **2019**, *10*, 4500.
[5] a) C. T. Campbell, *Nat. Chem.* **2012**, *4*, 597–598; b) H. T. Chung, D. A. Cullen, D. Higgins, B. T. Sneed, E. F. Holby, K. L. More, P. Zelenay, *Science* **2017**, *357*, 479–483; c) N. J. O'Connor, A. S. M. Jonayat, M. J. Janik, T. P. Senftle, *Nat. Catal.* **2018**, *1*, 531–539.
[6] G. Chen, P. Liu, Z. Liao, F. Sun, Y. He, H. Zhong, T. Zhang, E. Zschech, M. Chen, G. Wu, J. Zhang, X. Feng, *Adv. Mater.* **2020**, *32*, 1907399.
[7] R. Lang, W. Xi, J.-C. Liu, Y.-T. Cui, T. Li, A. F. Lee, F. Chen, Y. Chen, L. Li, L. Li, J. Lin, S. Miao, X. Liu, A.-Q. Wang, X.

Wang, J. Luo, B. Qiao, J. Li, T. Zhang, *Nat. Commun.* **2019**, *10*, 234.

[8] a) Q. Sun, N. Wang, T. Zhang, R. Bai, A. Mayoral, P. Zhang, Q. Zhang, O. Terasaki, J. Yu, *Angew. Chem. Int. Ed.* **2019**, *58*, 18570–18576; *Angew. Chem.* **2019**, *131*, 18743–18749; b) M. Yang, S. Li, Y. Wang, J. A. Herron, Y. Xu, L. F. Allard, S. Lee, J. Huang, M. Mavrikakis, M. Flytzani-Stephanopoulos, *Science* **2014**, *346*, 1498–1501.

[9] a) Y. Cheng, S. Zhao, B. Johannessen, J.-P. Veder, M. Saunders, M. R. Rowles, M. Cheng, C. Liu, M. F. Chisholm, R. De Marco, H.-M. Cheng, S.-Z. Yang, S. P. Jiang, *Adv. Mater.* **2018**, *30*, 1706287; b) J. Deng, H. Li, J. Xiao, Y. Tu, D. Deng, H. Yang, H. Tian, J. Li, P. Ren, X. Bao, *Energy Environ. Sci.* **2015**, *8*, 1594–1601; c) L. Wang, M.-X. Chen, Q.-Q. Yan, S.-L. Xu, S.-Q. Chu, P. Chen, Y. Lin, H.-W. Liang, *Sci. Adv.* **2019**, *5*, eaax6322.

[10] a) C.-C. Hou, L. Zou, L. Sun, K. Zhang, Z. Liu, Y. Li, C. Li, R. Zou, J. Yu, Q. Xu, *Angew. Chem. Int. Ed.* **2020**, *59*, 7384–7389; *Angew. Chem.* **2020**, *132*, 7454–7459; b) S. Yang, J. Zhang, L. Peng, M. Asgari, D. Stoian, I. Kochetygov, W. Luo, E. Oveisi, O. Trukhina, A. H. Clark, D. T. Sun, W. L. Queen, *Chem. Sci.* **2020**, *11*, 10991–10997.

[11] P. Peng, L. Shi, F. Huo, C. Mi, X. Wu, S. Zhang, Z. Xiang, *Sci. Adv.* **2019**, *5*, eaaw2322.

[12] a) C.-B. Ma, Y. Du, B. Du, H. Wang, E. Wang, *J. Colloid Interface Sci.* **2018**, *525*, 251–259; b) C.-B. Ma, Y. Zhang, Q. Liu, Y. Du, E. Wang, *Anal. Chem.* **2020**, *92*, 5319–5328; c) Y. Zhang, Q. Liu, C.-B. Ma, Q. Wang, M. Yang, Y. Du, *Theranostics* **2020**, *10*, 5064–5073.

[13] a) J. Fu, J. Dong, R. Si, K. Sun, J. Zhang, M. Li, N. Yu, B. Zhang, M. G. Humphrey, Q. Fu, J. Huang, *ACS Catal.* **2021**, *11*, 1952–1961; b) Y. Yang, Y. Qian, H. Li, Z. Zhang, Y. Mu, D. Do, B. Zhou, J. Dong, W. Yan, Y. Qin, L. Fang, R. Feng, J. Zhou, P. Zhang, J. Dong, G. Yu, Y. Liu, X. Zhang, X. Fan, *Sci. Adv.* **2020**, *6*, eaba6586.

[14] M. R. Horn, A. Singh, S. Alomari, S. Goberna-Ferron, R. Benages-Vilau, N. Chodankar, N. Motta, K. Ostrikov, J. MacLeod, P. Sonar, P. Gomez-Romero, D. Dubal, *Energy Environ. Sci.* **2021**, *14*, 1652–1700.

[15] a) G. Toupalas, J. Karlsson, F. A. Black, A. Masip-Sanchez, X. Lopez, Y. Ben M′Barek, S. Blanchard, A. Proust, S. Alves, P. Chabera, I. P. Clark, T. Pullerits, J. M. Poblet, E. A. Gibson, G. Izzet, *Angew. Chem. Int. Ed.* **2021**, *60*, 6518–6525; *Angew. Chem.* **2021**, *133*, 6592–6599; b) Y. Zhu, Y. Huang, Q. Li, D. Zang, J. Gu, Y. Tang, Y. Wei, *Inorg. Chem.* **2020**, *59*, 2575–2583.

[16] M. Stuckart, K. Y. Monakhov, *Chem. Sci.* **2019**, *10*, 4364–4376.

[17] a) Z. Han, Y. Gao, X. Zhai, J. Peng, A. Tian, Y. Zhao, C. Hu, *Cryst. Growth Des.* **2009**, *9*, 1225–1234; b) Z. A. Han, Y. L. Zhao, J. Peng, A. X. Tian, Q. Liu, J. F. Ma, E. B. Wang, N. H. Hu, *CrystEngComm* **2005**, *7*, 380–387.

[18] a) P. Bolle, H. Serier-Brault, R. Genois, E. Faulques, A. Boulmier, O. Oms, M. Lepeltier, J. Marrot, A. Dolbecq, P. Mialane, R. Dessapt, *J. Mater. Chem. C* **2016**, *4*, 11392–11395; b) S. Farhadi, M. M. Amini, M. Dusek, M. Kucerakova, F. Mahmoudi, *J. Mol. Struct.* **2017**, *1130*, 592–602; c) Y. Hu, H. An, X. Liu, J. Yin, H. Wang, H. Zhang, L. Wang, *Dalton Trans.* **2014**, *43*, 2488–2498; d) Y. Jia, S. Zhao, Y.-F. Song, *Appl. Catal. A* **2014**, *487*, 172–180; e) T. Li, H. N. Miras, Y.-F. Song, *Catalysts* **2017**, *7*, 260; f) M. A. Moussawi, N. Leclerc-Laronze, S. Floquet, P. A. Abramov, M. N. Sokolov, S. Cordier, A. Ponchel, E. Monflier, H. Bricout, D. Landy, M. Haouas, J. Marrot, E. Cadot, *J. Am. Chem. Soc.* **2017**, *139*, 12793–12803; g) C. Streb, R. Tsunashima, D. A. MacLaren, T. McGlone, T. Akutagawa, T. Nakamura, A. Scandurra, B. Pignataro, N. Gadegaard, L. Cronin, *Angew. Chem. Int. Ed.* **2009**, *48*, 6490–6493; *Angew. Chem.* **2009**, *121*, 6612–6615; h) M. Xu, B. Bi, B. Xu, Z. Sun, L. Xu, *Appl. Clay Sci.* **2018**, *157*, 86–91.

[19] a) W. G. Klemperer, in *Inorg. Synth.*, **1990**, pp. 74–85; b) Y. Xu, H. Yu, X. Jiang, J. Shi, B. Li, L. Li, L. Wu, M. Wang, *Chin. J. Chem.* **2022**, *40*, 813–818.

[20] Q. Cao, L.-L. Zhang, C. Zhou, J.-H. He, A. Marcomini, J.-M. Lu, *Appl. Catal. B* **2021**, *294*, 120238.

[21] Q. Shi, Y. Ji, W. Chen, Y. Zhu, J. Li, H. Liu, Z. Li, S. Tian, L. Wang, Z. Zhong, L. Wang, J. Ma, Y. Li, F. Su, *Natl. Sci. Rev.* **2020**, *7*, 600–608.

[22] F. Yang, P. Song, X. Liu, B. Mei, W. Xing, Z. Jiang, L. Gu, W. Xu, *Angew. Chem. Int. Ed.* **2018**, *57*, 12303–12307; *Angew. Chem.* **2018**, *130*, 12483–12487.

[23] P. Song, M. Luo, X. Liu, W. Xing, W. Xu, Z. Jiang, L. Gu, *Adv. Funct. Mater.* **2017**, *27*, 1700802.

[24] J. Geng, S. Zhang, H. Xu, G. Wang, H. Zhang, *Chem. Commun.* **2021**, *57*, 5410–5413.

[25] W. Chen, J. Pei, C.-T. He, J. Wan, H. Ren, Y. Zhu, Y. Wang, J. Dong, S. Tian, W.-C. Cheong, S. Lu, L. Zheng, X. Zheng, W. Yan, Z. Zhuang, C. Chen, Q. Peng, D. Wang, Y. Li, *Angew. Chem. Int. Ed.* **2017**, *56*, 16086–16090; *Angew. Chem.* **2017**, *129*, 16302–16306.

[26] C. Wang, D. Wang, S. Liu, P. Jiang, Z. Lin, P. Xu, K. Yang, J. Lu, H. Tong, L. Hu, W. Zhang, Q. Chen, *J. Catal.* **2020**, *389*, 150–156.

[27] Y. Zhu, Q. M. Ramasse, M. Brorson, P. G. Moses, L. P. Hansen, C. F. Kisielowski, S. Helveg, *Angew. Chem. Int. Ed.* **2014**, *53*, 10723–10727; *Angew. Chem.* **2014**, *126*, 10899–10903.

[28] Y. Wang, G. Jia, X. Cui, X. Zhao, Q. Zhang, L. Gu, L. Zheng, L. H. Li, Q. Wu, D. J. Singh, D. Matsumura, T. Tsuji, Y.-T. Cui, J. Zhao, W. Zheng, *Chem* **2021**, *7*, 436–449.

[29] M. Igisu, T. Yokoyama, Y. Ueno, S. Nakashima, M. Shimojima, H. Ohta, S. Maruyama, *Geobiology* **2018**, *16*, 412–428.

[30] X. He, X. Liu, B. Nie, D. Song, *Fuel* **2017**, *206*, 555–563.

[31] S.-I. Takekuma, M. Tamura, T. Minematsu, H. Takekuma, *Tetrahedron* **2007**, *63*, 12058–12070.

[32] C. Gong, X. Zeng, C. Zhu, J. Shu, P. Xiao, H. Xu, L. Liu, J. Zhang, Q. Zeng, J. Xie, *RSC Adv.* **2016**, *6*, 106248–106259.

[33] a) S. Fazil, R. Minitha, *Mater. Today Proc.* **2021**, *41*, 681–684; b) N. R. Pramanik, S. Ghosh, T. K. Raychaudhuri, R. J. Butcher, S. S. Mandal, *J. Coord. Chem.* **2011**, *64*, 1207–1215.

[34] Y. Zhou, X. Tao, G. Chen, R. Lu, D. Wang, M.-X. Chen, E. Jin, J. Yang, H.-W. Liang, Y. Zhao, X. Feng, A. Narita, K. Müllen, *Nat. Commun.* **2020**, *11*, 5892.

[35] a) P. P. Han, J. Li, C. L. Xing, M. Zhao, Q. X. Han, M. X. Li, *Inorg. Chem. Commun.* **2019**, *110*, 107592; b) T. Ouyang, X.-T. Wang, X.-Q. Mai, A.-N. Chen, Z.-Y. Tang, Z.-Q. Liu, *Angew. Chem. Int. Ed.* **2020**, *59*, 11948–11957; *Angew. Chem.* **2020**, *132*, 12046–12055.

[36] a) S. Bai, S. Hussain, C. Ge, M. S. Javed, S. Shah, G. Liu, G. Qiao, *Mater. Lett.* **2019**, *240*, 103–107; b) A. Kumar, S. Mukherjee, S. Sahare, R. K. Choubey, *Mater. Sci. Semicond. Process.* **2021**, *122*, 105471.

[37] Z. Y. Xiao, Y. C. Liu, J. Y. Zhang, D. X. Zhao, Y. M. Lu, D. Z. Shen, X. W. Fan, *Semicond. Sci. Technol.* **2005**, *20*, 796–800.

[38] M. Futsuhara, K. Yoshioka, O. Takai, *Thin Solid Films* **1998**, *322*, 274–281.

[39] D. Chang, Z. Zhao, W. Niu, L. Shi, Y. Yang, *Spectrochim. Acta Part A* **2021**, *260*, 119964.

[40] X. Liu, Y. Cheng, E. Liang, M. Chao, *Phys. Chem. Chem. Phys.* **2014**, *16*, 12848–12857.

[41] Y. Liu, J. Han, L. Fan, Y. Li, R. Guo, *Chem. Commun.* **2019**, *55*, 8064–8067.

[42] B. Xu, H. Wang, W. Wang, L. Gao, S. Li, X. Pan, H. Wang, H. Yang, X. Meng, Q. Wu, L. Zheng, S. Chen, X. Shi, K. Fan, X. Yan, H. Liu, *Angew. Chem. Int. Ed.* **2019**, *58*, 4911–4916; *Angew. Chem.* **2019**, *131*, 4965–4970.

[43] L. Gao, J. Zhuang, L. Nie, J. Zhang, Y. Zhang, N. Gu, T. Wang, J. Feng, D. Yang, S. Perrett, X. Yan, *Nat. Nanotechnol.* **2007**, *2*, 577–583.
[44] B. Xu, H. Wang, W. Wang, L. Gao, S. Li, X. Pan, H. Wang, H. Yang, X. Meng, Q. Wu, L. Zheng, S. Chen, X. Shi, K. Fan, X. Yan, H. Liu, *Angew. Chem. Int. Ed.* **2019**, *58*, 4911–4916; *Angew. Chem.* **2019**, *131*, 4965–4970.
[45] Q. Wang, T. Ina, W.-T. Chen, L. Shang, F. Sun, S. Wei, D. Sun-Waterhouse, S. G. Telfer, T. Zhang, G. I. N. Waterhouse, *Sci. Bull.* **2020**, *65*, 1743–1751.
[46] L. Jiao, W. Xu, Y. Zhang, Y. Wu, W. Gu, X. Ge, B. Chen, C. Zhu, S. Guo, *Nano Today* **2020**, *35*, 100971.
[47] a) C. X. Guo, X. T. Zheng, Z. S. Lu, X. W. Lou, C. M. Li, *Adv. Mater.* **2010**, *22*, 5164–5167; b) L. Jiao, W. Xu, H. Yan, Y. Wu, C. Liu, D. Du, Y. Lin, C. Zhu, *Anal. Chem.* **2019**, *91*, 11994–11999; c) M. Lian, X. Chen, Y. Lu, W. Yang, *ACS Appl. Mater. Interfaces* **2016**, *8*, 25036–25042.
[48] X. Shen, Z. Wang, X. Gao, Y. Zhao, *ACS Catal.* **2020**, *10*, 12657–12665.

Manuscript received: November 26, 2021
Accepted manuscript online: March 3, 2022
Version of record online: April 21, 2022